



# Non-invasive quantification of acute macrophagic lung inflammation with [<sup>11</sup>C](R)-PK11195 using a three-tissue compartment kinetic model in experimental acute respiratory distress syndrome

Laurent Bitker<sup>1,2,3</sup> · François Dhelft<sup>1</sup> · Sophie Lancelot<sup>3,4,5</sup> · Didier Le Bars<sup>3,4,5</sup> · Nicolas Costes<sup>3,4</sup> · Nazim Benzerdjeb<sup>6</sup> · Maciej Orkisz<sup>2</sup> · Jean-Christophe Richard<sup>1,2,3</sup>

Received: 23 September 2021 / Accepted: 30 January 2022 / Published online: 7 February 2022  
© The Author(s), under exclusive licence to Springer-Verlag GmbH Germany, part of Springer Nature 2022

## Abstract

**Purpose** Imaging of acute lung inflammation is pivotal to evaluate innovative ventilation strategies. We aimed to develop and validate a three-tissue compartment kinetic model (3TCM) of [<sup>11</sup>C](R)-PK11195 lung uptake in experimental acute respiratory distress syndrome (ARDS) to help quantify macrophagic inflammation, while accounting for the impact of its non-specific and irreversible uptake in lung tissues.

**Material and methods** We analyzed the data of 38 positron emission tomography (PET) studies performed in 21 swine with or without experimental ARDS, receiving general anesthesia and mechanical ventilation. Model input function was a plasma, metabolite-corrected, image-derived input function measured in the main pulmonary artery. Regional lung analysis consisted in applying both the 3TCM and the two-tissue compartment model (2TCM); in each region, the best model was selected using a selection algorithm with a goodness-of-fit criterion. Regional best model binding potentials (BP<sub>ND</sub>) were compared to lung macrophage presence, semi-quantified in pathology.

**Results** The 3TCM was preferred in 142 lung regions (62%, 95% confidence interval: 56 to 69%). BP<sub>ND</sub> determined by the 2TCM was significantly higher than the value computed with the 3TCM (overall median with interquartile range: 0.81 [0.44–1.33] vs. 0.60 [0.34–0.94],  $p < 0.02$ ). Regional macrophage score was significantly associated with the best model BP<sub>ND</sub> ( $p = 0.03$ ). Regional BP<sub>ND</sub> was significantly increased in the hyperinflated lung compartment, compared to the normally aerated one (median with interquartile range: 0.8 [0.6–1.7] vs. 0.6 [0.3–0.8],  $p = 0.03$ ).

**Conclusion** To assess the intensity and spatial distribution of acute macrophagic lung inflammation in the context of experimental ARDS with mechanical ventilation, PET quantification of [<sup>11</sup>C](R)-PK11195 lung uptake was significantly improved in most lung regions using the 3TCM. This new methodology offers the opportunity to non-invasively evaluate innovative ventilatory strategies aiming at controlling acute lung inflammation.

**Keywords** Acute respiratory distress syndrome · Positron emission tomography · [<sup>11</sup>C](R)-PK11195 · Inflammation · Ventilator-induced lung injury · Tissue compartment kinetic model

This article is part of the Topical Collection on Infection and inflammation

✉ Laurent Bitker  
laurent.bitker@chu-lyon.fr

<sup>1</sup> Service de Médecine Intensive – Réanimation, Hôpital de La Croix Rousse, Hospices Civils de Lyon, 103 Grande Rue de la Croix Rousse, 69004 Lyon, France

<sup>2</sup> Univ Lyon, INSA-Lyon, Université Claude Bernard Lyon 1, UJM-Saint Etienne, CNRS, Inserm, CREATIS UMR 5220, U1294, F-69621 Villeurbanne, France

<sup>3</sup> Université Lyon 1 Claude Bernard, Lyon, France

<sup>4</sup> CERMEP – Imagerie du Vivant, Lyon, France

<sup>5</sup> Hospices Civils de Lyon, Lyon, France

<sup>6</sup> Centre d'Anatomie Et Cytologie Pathologique, Centre Hospitalier Lyon Sud, Hospices Civils de Lyon, Lyon, France

## Introduction

The development of novel ventilatory strategies aiming at reducing ventilator-induced lung inflammation requires high-performance functional imaging of acute lung inflammation. [ $^{11}\text{C}$ ](R)-PK11195 is a specific ligand of the translocator protein (TSPO, or peripheral benzodiazepine receptor), expressed by the mitochondria of macrophages [1]. The radiotracer has been mostly used to evaluate macrophagic inflammation in clinical and experimental models of central nervous system, vascular or articular inflammation [1–6]. To date, [ $^{11}\text{C}$ ](R)-PK11195 studies have used a plasma-input two-tissue compartment kinetic model (2TCM) to describe the tracer's uptake [4–7].

Our research group recently published the first usage of [ $^{11}\text{C}$ ](R)-PK11195 to evaluate acute lung inflammation triggered by high tidal volume ventilation in healthy swine lungs, quantified by the mean of standardized uptake values (SUV) [8]. However, since the lung has a large blood compartment and major regional tissue heterogeneity, kinetic model may be a more appropriate to effectively quantify macrophage inflammation. Development of a kinetic model is also warranted by the high non-specific uptake of [ $^{11}\text{C}$ ](R)-PK11195 in tissues due to its high lipophilicity [7, 9].

We hypothesized that [ $^{11}\text{C}$ ](R)-PK11195 is prone to irreversible and non-specific accumulation in tissues, trapped in the cellular bilayer lipidic membrane due to its high lipophilicity [9]. Tracer kinetics would then be better described using a plasma-input 3-tissue compartment kinetic model (3TCM) with an irreversible compartment, compared to the traditional 2TCM that is usually used to describe this radiotracer's uptake in tissues [5, 7]. The main objective of our study was to develop and validate a 3TCM of [ $^{11}\text{C}$ ](R)-PK11195 lung uptake in a swine experimental model of acute respiratory distress syndrome.

## Materials and methods

### 3TCM of [ $^{11}\text{C}$ ](R)-PK11196 lung uptake

Lung [ $^{11}\text{C}$ ](R)-PK11195 uptake is described using a three-tissue compartment pharmacokinetic model (Fig. 1), using a [ $^{11}\text{C}$ ](R)-PK11195 parent plasma input function (IF)  $C_{\text{PK}}(t)$ , and the PET time-activity curve (TAC) in the lung region-of-interest  $C_{\text{ROI}}(t)$  as the model inputs. The model encompasses 3 tissue compartments representing the concentration of [ $^{11}\text{C}$ ](R)-PK11195 free in tissue,  $C_f(t)$ ; TSPO-bound in tissue,  $C_b(t)$ ; and irreversibly and non-specifically bound in tissue,  $C_{\text{ns}}(t)$  (presumably by

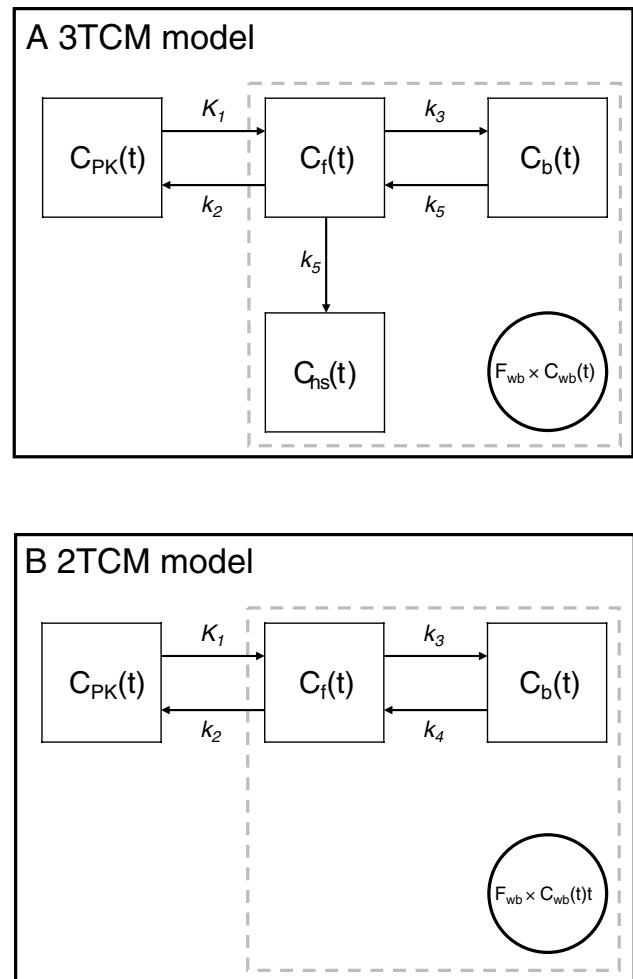


**Fig. 1** [ $^{11}\text{C}$ ](R)-PK11195 pharmacokinetic compartment models. Panel **A** shows the 3-compartment kinetic model of [ $^{11}\text{C}$ ](R)-PK11195 uptake in the lung, using a plasma input function  $C_{\text{PK}}(t)$ .  $C_f(t)$  is the concentration of free parent tracer in lung tissue over time (compartment #1),  $C_b(t)$  is the concentration of parent compound bound to the TSPO receptor in the ROI over time (compartment #2), and  $C_{\text{ns}}(t)$  is the concentration of tracer non-specifically and irreversibly trapped in the tissue over time (compartment #3).  $F_{\text{WB}} \times C_{\text{wb}}(t)$  represents the fractional concentration of whole blood present in the ROI over time. The lung ROI is represented by the dashed gray line. Rate constants  $k_x$  are associated with arrows showing the direction of the kinetic transfer they describe. Panel **B** shows the two-tissue compartment model (2TCM), with the same design as the model presented in panel **A**, without the irreversible non-specific compartment. ROI, region of interest; 2TCM, two-tissue compartment model; 3TCM, three-tissue compartment model; TSPO, translocator protein

lipophilic compounds such as cell membranes). An additional parameter  $F_{\text{WB}}$  relates to the vascular whole blood (without correction for the plasma fraction and metabolites) fractional radioactive concentration  $C_{\text{wb}}(t)$  in the region-of-interest (ROI).

The model requires the determination of  $F_{\text{WB}}$  and five rate constants  $K_1, k_2, k_3, k_4$ , and  $k_5$  which are the entry rate constant from blood to tissue ( $K_1$  in  $\text{ml of plasma min}^{-1} \text{ ml}^{-1}$

of lung, the backward rate constant of transfer from tissue to blood ( $k_2$  in  $\text{min}^{-1}$ ), the rate constant representing [ $^{11}\text{C}$ ](R)-PK11195 binding to the TSPO receptor ( $k_3$  in  $\text{min}^{-1}$ ), the rate constant corresponding to its dissociation from its receptor ( $k_4$  in  $\text{min}^{-1}$ ), and the rate constant of irreversible uptake by the non-specific compartment ( $k_5$  in  $\text{min}^{-1}$ ). The non-displaceable binding potential  $\text{BP}_{\text{ND}}$  of [ $^{11}\text{C}$ ](R)-PK11195 by the 3TCM was computed as the ratio of  $k_3$  to  $k_4$ .  $\text{BP}_{\text{ND}}$  corresponds to the ratio of specifically bound [ $^{11}\text{C}$ ](R)-PK11195 to its non-displaceable concentration in tissue at equilibrium [10].

## 2TCM of [ $^{11}\text{C}$ ](R)-PK11196 lung uptake

To evaluate the performance of the 3TCM, we used the 2TCM (Sokoloff) model, which is the most commonly used kinetic model to describe the reversible association of [ $^{11}\text{C}$ ](R)-PK11195 to TSPO in tissues (Fig. 1) [7]. The 2TCM was similar to the 3TCM, with the exception of the non-specific irreversible compartments, and requires the determination of 4 rate constants  $K_1$ ,  $k_2$ ,  $k_3$ ,  $k_4$ , and  $F_{\text{WB}}$ , which have the same definition as for the 3TCM.

## Model comparison

To determine the model that best described the lung regional TACs of [ $^{11}\text{C}$ ](R)-PK11195, we applied the 3TCM and the 2TCM to all lung ROIs, and then applied a 2-step model selection algorithm described in Fig. 2. We first calculated their respective value of the corrected Akaike information criterion (AICc); the best model was that with the lowest AICc value [11]. Second, for ROIs in which the value of  $k_4$  determined by the 2TCM was near zero (i.e.,  $k_4 < 10^{-6} \text{ min}^{-1}$ ), 3TCM was considered the most appropriate model, even if AICc favored the 2TCM over the 3TCM. This strategy was justified based on our hypothesis that very low  $k_4$  values would lead to unrealistically high values of  $\text{BP}_{\text{ND}}$ , conceptually incompatible with reversible binding and potentially reflecting the existence of an irreversible compartment unaccounted for the model.

From this point onwards, the model selected by the algorithm is designated as the “best model,” and ROIs are characterized as being of 2TCM- or 3TCM-type. To assess the magnitude of the deviation in goodness-of-fit, their difference was calculated for each ROI ( $\text{DAICc} = \text{AICc}_{2\text{TCM}} - \text{AICc}_{3\text{TCM}}$ ). In case of a 2TCM-type TAC (in which no  $k_5$  is computed by design), a theoretical  $k_5$  was considered equal to  $0 \text{ min}^{-1}$ .

## Description of experimental protocols

We used the data from 2 studies evaluating the effects of various ventilatory strategies on lung mechanics and

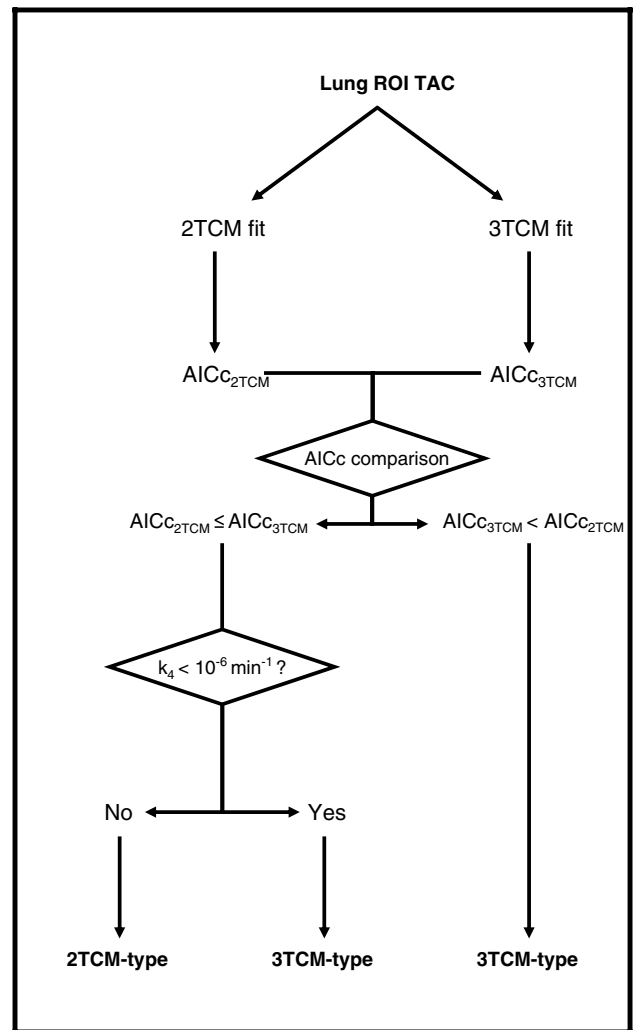


**Fig. 2** Model selection algorithm. The figure describes the step-by-step process by which a lung ROI was identified as being of the 2TCM-type or of the 3TCM-type, based on a 2-step selection algorithm. 2TCM, two-tissue compartment model; 3TCM, three-tissue compartment kinetic model; AIC, corrected Akaike information criterion; ROI, region of interest; TAC, time-activity curve

inflammation in animals with experimental ARDS. The protocols were approved by an animal ethics committee (CELYNE, reference no. 2015041015179195 and 201,907,311,141,381). Pigs weighing 29 [27–30] kg were maintained during all experiments under continuous general anesthesia (propofol and fentanyl) and neuromuscular blockade (cisatracurium). The animals were equipped with a pulmonary artery catheter used to perform invasive sampling of the input function directly in the pulmonary artery. Experimental acute respiratory distress syndrome was performed by the mean of intra-tracheal instillation of 0.1 M of hydrochloric acid (3 to 5 ml  $\text{kg}^{-1}$  of body weight) [12]. Details on animal conditioning, experimental ARDS, and mechanical ventilation are presented in Supplemental methods 1. The

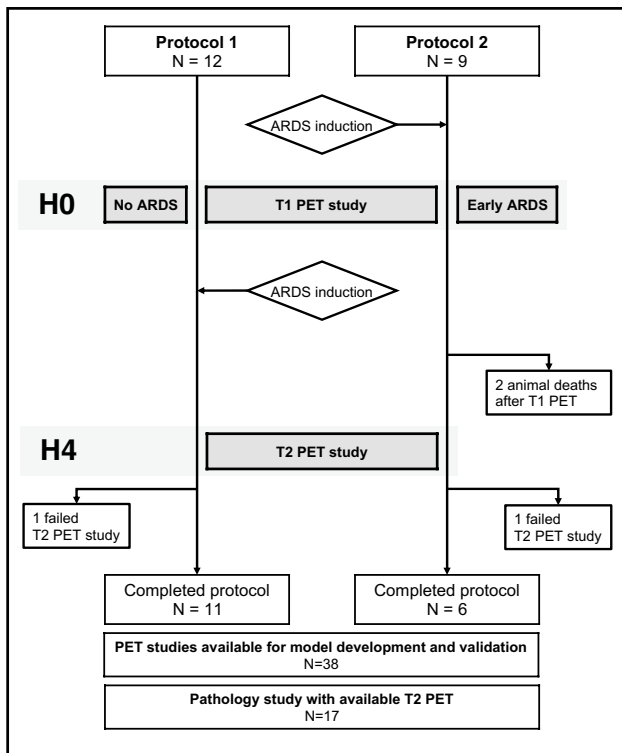


**Fig. 3** Study flowchart. The figure summarizes main protocol steps and the number of animals studied at each study step. Protocol 1 consisted of 2 PET/CT studies that evaluated animals before experimental ARDS, and after 4 h of experimental ARDS, with half of animals randomized to be prone for 4 h. In protocol 2, the first PET acquisitions were performed immediately after ARDS induction, and again after 4 h, with half of animals randomized to receive ultra-low tidal volume ventilation, compared to conventional protective ventilation. Hence, in T1 PET studies, 2 types of experimental conditions were defined: *no ARDS* corresponding to PET studies performed on healthy lungs (protocol 1), and *early ARDS* corresponding to PET studies on injured lungs immediately after ARDS induction (protocol 2). At T2, all animals had experimental ARDS by design. In both protocols, H0 corresponded to the end of the first PET study, from which the 4-h study period started. Successful protocols ended with surgical lung extraction and pathology study of lung samples. Animal deaths in protocol 2 were related to refractory vasoplegic shock. Failed T2 PET studies were related to failed [ $^{11}\text{C}$ ](R)-PK11195 radiosynthesis. ARDS, acute respiratory distress syndrome; PET, positron emission tomography

first lung PET acquisition (T1) was performed either before (no ARDS) or immediately after experimental ARDS (early ARDS), and again 4 h later (T2, late ARDS, Fig. 3).

### PET acquisition protocol and PET-CT post-processing

For all PET acquisitions, we used a Siemens Biograph TruePoint PET/CT (Siemens, Germany). [ $^{11}\text{C}$ ](R)-PK11195 synthesis was performed on site as previously described, using a C-11 Pro2 synthesizer (iPHASE, Melbourne, Victoria, Australia) [13]. Radiochemical purity at the end of

radiosynthesis was  $>99\%$ . PET acquisitions lasted 60 min, starting at the onset of the [ $^{11}\text{C}$ ](R)-PK11195 injection (body weight dose of  $4.8 [4.0\text{--}5.7] \text{ MBq kg}^{-1}$ ). The radiotracer was administered on the proximal port of the central venous line, at a rate of  $20 \text{ ml min}^{-1}$  over 30 s in animals of protocol 1, and at a rate of  $10 \text{ ml min}^{-1}$  over 60 s for protocol 2. PET acquisitions were a dynamic series of 18 frames with increasing durations:  $5 \times 12 \text{ s}$ ,  $4 \times 60 \text{ s}$ ,  $7 \times 300 \text{ s}$ , and  $2 \times 600 \text{ s}$ . The 216-mm longitudinal field-of-view extended over the whole lung area, from the most caudal extremity in sagittal view to the apex. PET frames were reconstructed in 3D volumes of 112 slices (thickness 2 mm) with in-plane  $128 \times 128$  matrices ( $2.1 \times 2.1 \text{ mm}$  pixel size). Data were corrected for random coincidences, attenuation (using the preceding transmission CT with similar reconstruction parameters), scatter, and  $^{11}\text{C}$  isotope decay.

Transmission CTs were used to segment PET data, and extract lung density and aeration, using OsiriX (Bernex, Switzerland), excluding intrathoracic large vessels and large airways [14]. From the volumetric masks, we computed PET TACs in 6 distinct lung regions (anatomical segmentation in the antero-posterior and cephalo-caudal axes, Supplemental Fig. 1), and in 4 aeration clusters (nonaerated ( $-100$  to  $+100$  Hounsfield units), poorly aerated ( $-500$  to  $-101$  HU), normally aerated ( $-900$  to  $-501$  HU), and hyperinflated ( $-1000$  to  $-901$  HU)) [15].  $F_D$  was computed using the X-ray attenuation of the transmission CT scan [15]. Image post-processing was performed using MatLab (Natick, MA, USA) dedicated scripts. Details on image post-processing are presented in Supplemental methods 2.

### Resolution method of the 3TCM and 2TCM models

The 3TCM can be expressed and resolved using the differential equations presented in Supplementary methods 3. Using convolution, non-linear least-square resolution was performed using the [ $^{11}\text{C}$ ](R)-PK11195 parent plasma input function  $C_{PK}(t)$ , the lung ROI TAC  $C_{ROI}(t)$ , and a whole blood input function  $C_{WB}(t)$  for  $F_{WB}$  determination. The initial guesses of rate constants  $K_1$ ,  $k_2$ ,  $k_3$ ,  $k_4$ ,  $k_5$ , and  $F_{WB}$  were  $1 \text{ ml min}^{-1} \text{ ml lung}^{-1}$ ,  $0.4 \text{ min}^{-1}$ ,  $0.01 \text{ min}^{-1}$ ,  $0.04 \text{ min}^{-1}$ ,  $0.001 \text{ min}^{-1}$ , and  $0.05$ , respectively. The initial guess of  $K_1$  was corrected for the computerized tomography (CT)-measured lung density  $F_D$  to account for its heterogeneity in different ROIs [15].  $k_2$  initial guess was changed to  $0.25 \text{ min}^{-1}$  in case of out-of-range values of microparameters  $k_3$  ( $>100 \text{ min}^{-1}$ ) [16]. The regression algorithm used trust-region reflective algorithm, aiming to minimize the sum of squares between fitted and observed values, i.e.,  $C_{ROI}(t)$ , with weighting by PET frame length. Fitted parameters, including  $F_{WB}$ , were all constrained between 0 and  $+\infty$ . Non-linear least-square resolution of the 2TCM was performed using the exact same methodology as for the

3TCM (using the same initial guesses and constraints of rate constants, with the exclusion of  $k_5$ ).  $BP_{ND}$  was computed similarly to the 3TCM.

Regional SUV in each lung ROIs was computed using the mean radioactivity measured between 40 and 60 min after injection [17], and was corrected by  $F_D$ , to take into account lung aeration [18].

## Model input function

The methodology of the image-derived plasma parent input function (IF)  $C_{PK}(t)$  and whole blood input function  $C_{WB}(t)$  determinations is fully described in Supplemental methods 4. Briefly, an invasive IF was obtained during all experiments by the mean of pulmonary arterial blood repetitive sampling, using a Wizard<sup>2</sup> gamma counter (PerkinElmer, MA, USA) cross-calibrated with the PET camera. Then, we obtained an image-derived input function, by drawing a 1-cm<sup>3</sup> ROI in the main pulmonary artery on the PET image, which was secondarily corrected for partial volume and spill-over phenomena using two invasive IF measurements [19]. From the invasive IF measurements, we also computed a plasma to blood radioactivity ratio over time  $f_p(t)$ . Also, we computed a parent fraction over time of [<sup>11</sup>C](R)-PK11195  $f_{PK}(t)$  using a population model fit of individual metabolite data [3]. Finally, a radiotracer regional tissue arrival delay into the lung ROI was computed using a single-compartment reversible pharmacokinetic model, including a blood fraction compartment, fitted over the first 60 s of the ROI TAC. After correction for spillover, partial volume, and regional arrival delay, the image-derived IF corresponded to  $C_{WB}(t)$  and was multiplied by  $F_{WB}$  during model resolution to reflect the vascular compartment in the PET image. It hence accounted for the total radioactivity of parent compound and its metabolites present in blood cells and plasma. To compute the plasma parent IF  $C_{PK}(t)$ ,  $C_{WB}(t)$  was multiplied by  $f_p(t)$  and  $f_{PK}(t)$ .

## Monte Carlo error simulations

Simulations were performed to investigate the effects of varying values of regional  $F_D$ , regional tissue arrival delay in lung ROI, spillover coefficient (SC), and [<sup>11</sup>C](R)-PK11195 parent fraction over time  $f_{PK}(t)$  on  $BP_{ND}$  bias. Bias was defined as the relative difference between the fitted value of  $BP_{ND}$  and its theoretical (ideal) value, in % [7]. For this, a representative image-derived parent plasma IF was used to generate an ideal lung TAC using the 3TCM and the following set of parameters:  $K_l = 3.2$  ml of plasma  $\text{min}^{-1}$   $\text{ml}^{-1}$  of lung,  $k_2 = 1.1$   $\text{min}^{-1}$ ,  $k_3 = 0.04$   $\text{min}^{-1}$ ,  $k_4 = 0.05$   $\text{min}^{-1}$ ,  $k_5 = 0.003$   $\text{min}^{-1}$ ,  $F_{WB} = 0.14$ ,  $BP_{ND} = 0.73$ , spillover coefficient =  $2.1 \times 10^{-5}$   $\text{min}^{-1}$ , regional arrival delay = 3.7 s, parent

fraction  $\alpha$  coefficient = 0.15. These values of  $k_3$  and  $k_4$  were used to calculate an ideal  $BP_{ND}$  value.

For simulation purposes, parameter range of variation was 0.1 to 0.9 for  $F_D$ , 0 to 6 s for tracer regional arrival delay in ROI, 10th percentile to 90th percentile of observed SC values, and 0.01 to 0.5 for the  $\alpha$  coefficient of [<sup>11</sup>C](R)-PK11195 parent fraction model (corresponding to a 1 to 50% fraction of remaining parent compound at 60 min). For each level of the varying parameter, a new TAC was generated with the addition of a 5% or a 10% Gaussian noise to the data, leading to the generation of 1000 TACs with 2 levels of Gaussian noise. Subsequently, fit using the 3TCM was performed on each simulated noisy TAC. Hence, thousand values of simulated binding potentials generated from the simulated curves were compared to the ideal  $BP_{ND}$ , to compute the relative bias and coefficient of variation at each level of the studied parameter. Also, using the ideal TAC generated with the 3TCM, and to which a 10% Gaussian noise was added, we also evaluated the mean bias generated if a 2TCM was applied. Finally, a similar methodology was applied to evaluate the impact of PET image noise on the frequency of ROI classification to the 3TCM type based on the low  $k_4$  criterion.

## Pathology study

After the second PET acquisition, animals were euthanized and their lungs were surgically extracted for pathology analysis. The right lung was divided into 6 regions, reproducing the pattern used to segment PET images. A cubic centimeter sample of each lung region was prepared for pathology analysis with hematoxylin and eosin staining. Macrophage presence was evaluated using a semi-quantitative score, ranging from 0 to 3 (Supplementary methods 5). Neutrophil counts in both the alveolar and interstitial lung compartments were quantified using an ordinal scale ranging from 0 to 2 (0 if no neutrophils were identified, 1 if 1 to 5 neutrophils were present in the field-of-view, and 2 if > 5 neutrophils were present) [12]. Histologic lung injury was quantified using a semi-quantitative score also presented in Supplementary methods 5 [20]. All scores were evaluated on 5 to 20 random fields-of-view at 10× and 40× magnification by a pathologist blinded to study protocols and model results. Pathology scores were compared to  $BP_{ND}$  measured on the second PET acquisition.

## Statistics

A  $p$  value below 0.05 was chosen for statistical significance. All analyses were performed using R [21]. All quantitative variables are reported using median and interquartile range in brackets, except stated otherwise, and categorical variables with count and percentage in parenthesis. We reported



the ratio of median absolute deviation to median as an indicator of the variable dispersion.

Association of lung regions, experimental conditions, aeration levels, or pathology results with regional  $BP_{ND}$  (or other regionally measured variables of interest) were performed using mixed-effects regression models to evaluate the association of variables of interest (fixed effects) with the dependent variable, using the animal number as random effect to account for the repetition of regional measurements in each animal. Interactions were systematically evaluated; in the case of a significant interaction, a post hoc analysis using pairwise comparison adjusted for the repetition of statistical tests was performed using the Tukey method. In the case of a linear association between 2 variables in a model including a random effect, we produced the marginal  $R^2$  value evaluating the strength of the correlation between the fixed effect and the dependent variable, independently from the random effect. In the case of post hoc multiple comparisons to a single reference level, we used the Dunnett adjustment method. Finally, all model  $p$  values were calculated using parametric bootstrapping with 500 simulated values.

## Results

Twenty-one animals were included, comprising 38 PET acquisitions (Fig. 3). The details of parent plasma input function determination of  $[^{11}C](R)$ -PK11195 are presented in Supplemental Results 1.

### Performance of model selection using the algorithm

Based on the selection algorithm, the 3TCM was preferred in 62% ( $N=142/228$ , 95% confidence interval: 56 to 69%) of lung ROIs, and the 2TCM preferred in 38% of ROIs ( $N=86/228$ , Supplemental Fig. 2). Figure 4 shows illustrative fits with both models (Supplemental Fig. 3 for residual analysis of all fitted regional TAC). Frequency of 3TCM selection significantly differed between lung regions, but not between experimental conditions (Supplemental Fig. 2).

### Impact of the low $k_4$ criterion for 3TCM ROI classification

3TCM was selected based on the low  $k_4$  criterion in 7% ( $N=16/142$ ) of 3TCM-type ROIs. Normalized root mean squared error (nRMSE) of low  $k_4$  3TCM-type ROIs was significantly higher than the nRMSE of 2TCM-type ROIs (Fig. 5).  $k_5$  of  $\Delta AICc$ - and low  $k_4$ -classified 3TCM-type ROIs were significantly different from 0, and significantly higher than the  $k_5$  computed by the 3TCM in 2TCM-type ROIs (Fig. 5). Increasing image noise increased the frequency of misclassification to 2TCM, with the low  $k_4$

criterion allowing correct reclassification in 23% of simulated cases at maximum simulated noise level (Fig. 5D). Finally, increasing 3TCM-type regional  $k_5$  values were linearly associated with increasing  $\Delta AICc$  values (Supplemental Fig. 4).

### 2TCM, 3TCM, and best model parameters

Best model estimates (with ratio of median absolute deviation to median between parenthesis) were the following:  $K_1=2.4$  [1.3–3.8]  $\text{ml min}^{-1} \text{ml lung}^{-1}$  (0.48);  $k_2=0.7$  [0.5–0.9]  $\text{min}^{-1}$  (0.30);  $k_3=0.07$  [0.03–0.17]  $\text{min}^{-1}$  (0.69);  $k_4=0.13$  [0.06–0.27]  $\text{min}^{-1}$  (0.64);  $k_5=0.002$  [0.00–0.008]  $\text{min}^{-1}$  (1.23);  $BP_{ND}=0.56$  [0.31–0.90] (0.50);  $F_{WB}=0.06$  [0.04–0.10] (0.49). In 3TCM-type ROIs, median  $k_5$  was 0.006 [0.002–0.01]  $\text{min}^{-1}$ . Supplemental Fig. 5 shows the correlation between best model rate constants and the 2TCM rate constants in all ROIs. When comparing models' results in the same ROI,  $BP_{ND}$  values estimated by the 2TCM were significantly higher than those estimated by the 3TCM (0.81 [0.44–1.33] vs. 0.60 [0.34–0.94]), or that of the best model (0.56 [0.31–0.90],  $p=0.02$  for both comparisons to the 2TCM value). Finally,  $BP_{ND}$  showed a weak correlation with  $F_D$ -corrected SUV (Fig. 6).

### Association of best model BPND with pathology

Regional distribution of macrophage recruitment, neutrophils count, and the lung injury score ( $N=102$  samples) significantly differed between lung regions (Supplemental Fig. 6). Best model  $BP_{ND}$  was significantly associated with the macrophage score, but not with the lung injury score or neutrophil counts in the alveolar space or the interstitium (Fig. 7). The association of  $BP_{ND}$  with the macrophage score was not significant if using exclusively 2TCM-derived  $BP_{ND}$  (Supplemental Fig. 7).

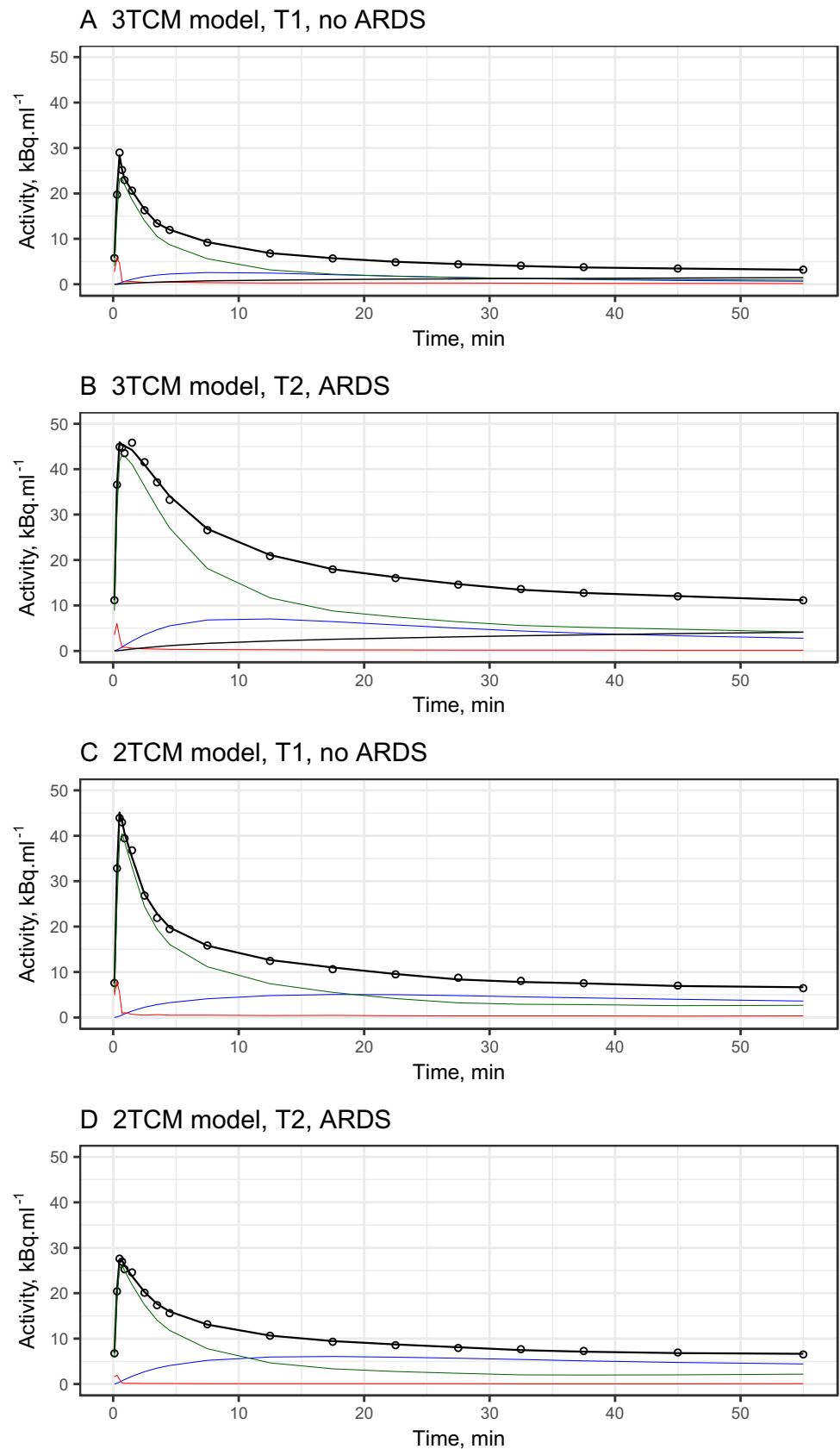
### Effect of experimental ARDS and lung aeration on BPND

At T1, best model  $BP_{ND}$  was significantly increased in case of *early ARDS*, compared to normal lungs, and significantly varied between lung ROIs (Supplemental table 1). When considering T1 and T2 data, best model  $BP_{ND}$  was significantly higher in the hyperinflated and the nonaerated lung compartments, compared to the normally aerated compartment (Fig. 8).

### Results of Monte Carlo error simulations

$BP_{ND}$  biases resulting from simulated TACs are presented in Fig. 9. First, the 2TCM led to  $27 \pm 6\%$  overestimation of  $BP_{ND}$  value when applied to a 3TCM-type simulated

**Fig. 4** Curve fits with the 3TCM and 2TCM models. The figure shows the fits obtained using the 3TCM in a 3TCM-type ROI (**A** and **B**), and using the 2TCM model in 2TCM-type ROI (**C** and **D**). Panels **A** and **C** correspond to fits performed on ROIs without experimental ARDS at T1, and panels **B** and **D** in ROIs with experimental ARDS at T2 (late ARDS). The green line is the concentration of free parent tracer in lung tissue  $C_f(t)$ , the blue line is the concentration of parent compound bound to the TSPO receptor in the ROI  $C_b(t)$ , and the red line is the amount of radioactivity in the whole blood within the ROI  $C_{wb}(t)$ . In panel **A** and **B**, the light black line is the concentration of tracer non-specifically and irreversibly trapped in the tissue  $C_{ns}(t)$ . The open dots are the lung ROI PET radioactivity measurements, and the heavy black line is the sum of the individual compartmental concentrations computed over time. ARDS, acute respiratory distress syndrome; PET, positron emission tomography; ROI, region of interest; 2TCM, two-tissue compartment model; 3TCM, three-tissue compartment kinetic model



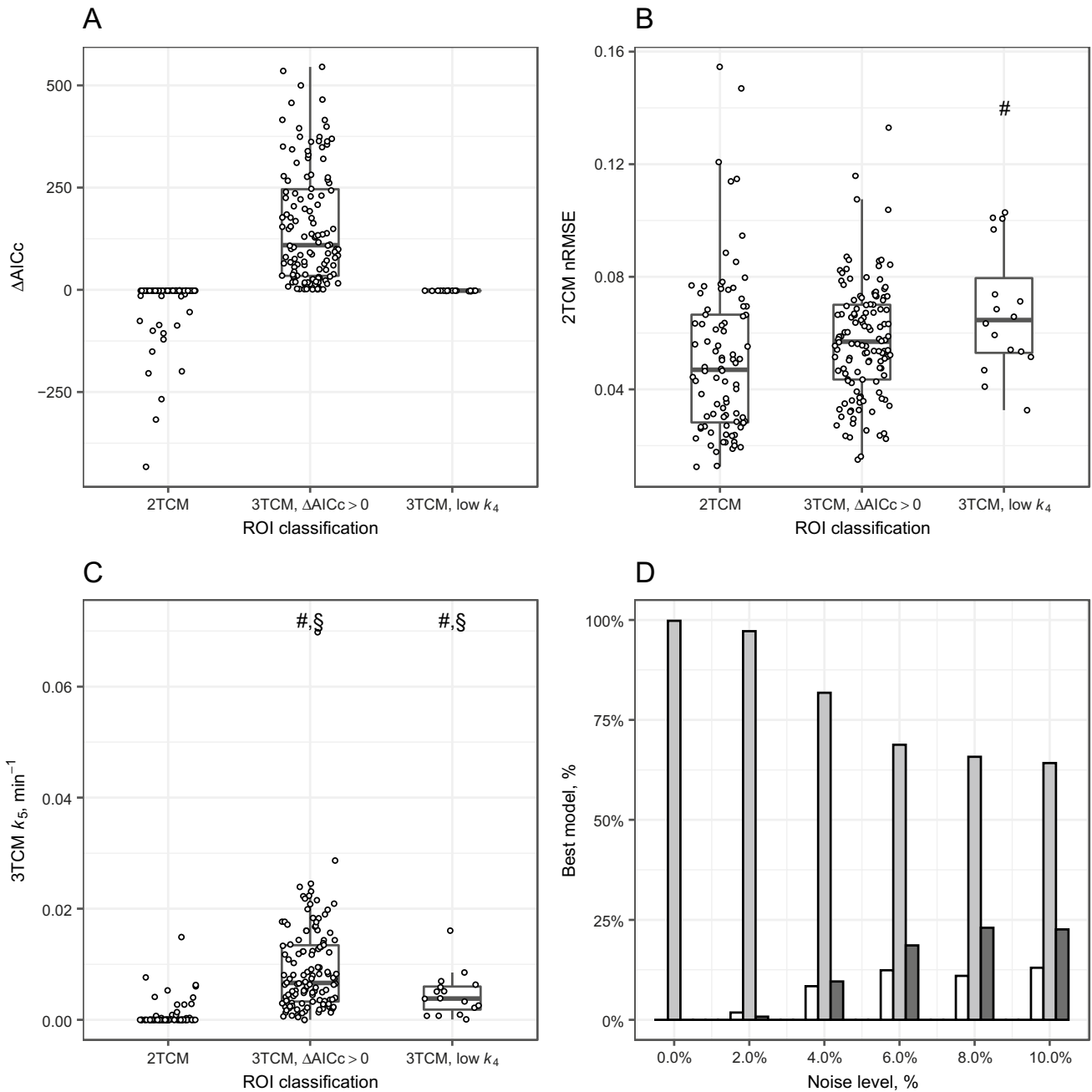


**Fig. 5** Association of the low  $k_4$  criterion for classification to 3TCM type on model goodness of fit,  $k_5$  values, and simulated image noise. The figure shows the  $\Delta AICc$  value (A), 2TCM normalized root mean squared error (B), and the 3TCM  $k_5$  constant rate (C) in all ROIs, separated based on the kinetic model they were classified to, and the result of increasing image noise simulations on kinetic model selections rates. 3TCM criteria of selection ( $\Delta AICc$  or low  $k_4$ ) are presented. In panels B and C, the hashtag indicates a significant difference ( $p < 0.05$ ) in 2TCM nRMSE or  $k_5$  values with 2TCM-type ROIS (post hoc pairwise multiple comparison). In panel C, the § sign indi-

cates that  $k_5$  of 3TCM-type ROIs were significantly different from 0 ( $p < 0.05$ ). Panel D represents the results of ROI classification (2TCM in white,  $\Delta AICc$  3TCM in light gray, and low  $k_4$  3TCM in dark gray) of simulated noisy PET TAC of a 3TCM-type ROI, with noise increasing from 0 to a 10% Gaussian noise.  $\Delta AICc$ , difference in corrected Akaike information criterion; nRMSE, normalized root mean squared error; PET, positron emission tomography; ROI, region of interest; 2TCM, two-tissue compartment model; 3TCM, three-tissue compartment kinetic model

TAC. Also,  $BP_{ND}$  bias was kept constant across all  $F_D$  values. Mean  $BP_{ND}$  bias was within  $\pm 15\%$  with varying tissue arrival delay, and reached a maximum of  $-40\%$  with the



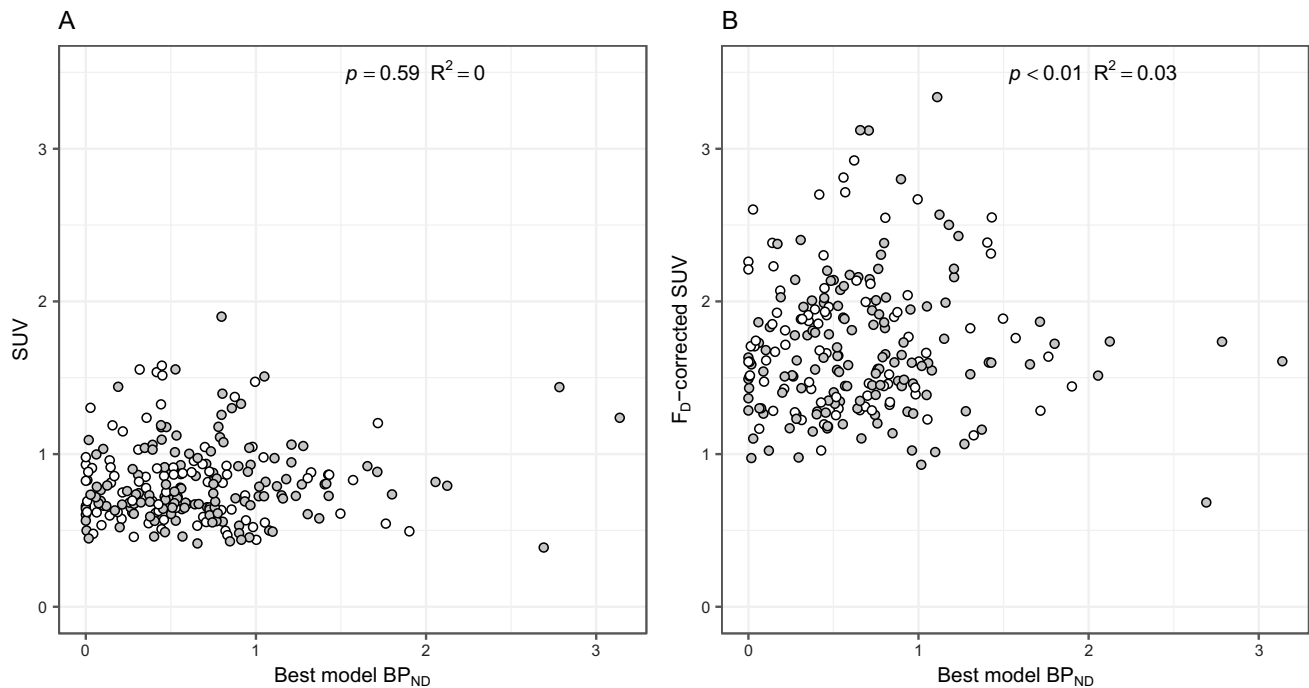


**Fig. 6** Association of [<sup>11</sup>C](R)-PK11195 binding potential with region SUV with or without normalization to lung ROI density. The figure shows the association of regional best model BP<sub>ND</sub> with uncorrected (panel **A**) and F<sub>D</sub>-corrected SUV (**B**). Each regional estimate is represented, in gray for BP<sub>ND</sub> derived from the 3TCM model, and

in white for those derived from the 2TCM model. The *p* value examines the linear association between BP<sub>ND</sub> and the variable of interest. BP<sub>ND</sub>, binding potential; F<sub>D</sub>, lung ROI density; SUV, standardized uptake value

highest SC values. Low and high values of parent fraction  $\alpha$  led to the highest degree of BP<sub>ND</sub> bias.

## Discussion

In the present study, we evaluated the performance of a plasma-input 3TCM pharmacokinetic model of [<sup>11</sup>C](R)-PK11195 uptake in the lungs of animals with and without experimental ARDS. Our results show that (1) the 3TCM was more frequently selected as the most appropriate model, compared to the conventional 2TCM; (2) regional BP<sub>ND</sub> significantly increased with lung macrophage infiltration in pathology, supporting the radioligand's specificity to evaluate acute macrophagic lung inflammation in PET; and (3) regional BP<sub>ND</sub> was significantly increased in hyperinflated lung regions, suggesting its performance to evaluate VILI.

Experience of plasma-input kinetic models of [<sup>11</sup>C](R)-PK11195 in the lung is poor. To date, this is the first study to evaluate multiple plasma-input kinetic models of [<sup>11</sup>C](R)-PK11195 in lungs with or without experimental ARDS. PET imaging of the lungs is especially challenging due to the heterogeneity of the studied tissue (amplified in case of ARDS), due to the presence of air and blood in the ROI, the very large size of ROI when studying the whole organ, and

finally the existence of movement during image acquisition, among others [22].

Our results show that, with our methodology, BP<sub>ND</sub> was superior to SUV and F<sub>D</sub>-corrected SUV to quantify [<sup>11</sup>C](R)-PK11195 lung uptake, which strongly supports that compartmental modeling is warranted to accurately quantify specific [<sup>11</sup>C](R)-PK11195 lung uptake. Also, our results were independent from lung density variations, which is a major asset when evaluating a high heterogeneous organ such as the lung. Furthermore, we demonstrate the superiority of the 3TCM over the 2TCM, as the latter led to an estimated 27% bias in the radioligand lung uptake in our simulation study. Extrinsic validity of the model is supported by the fact that regional BP<sub>ND</sub> was significantly increased in case of experimental ARDS, but also augmented in the most hyperinflated lung regions, as well as in nonaerated ones. This important finding implies that [<sup>11</sup>C](R)-PK11195 kinetic model is potentially capable of investigating the impact of ventilation on lung parenchyma, in parallel with the examination of the disease severity.

Our work demonstrates the frequent superiority of the 3TCM in terms of fit quality and model selection by the algorithm, compared to the 2TCM. The addition of a third compartment is also supported by the fact that it allowed adequate model determination in the case of impossible

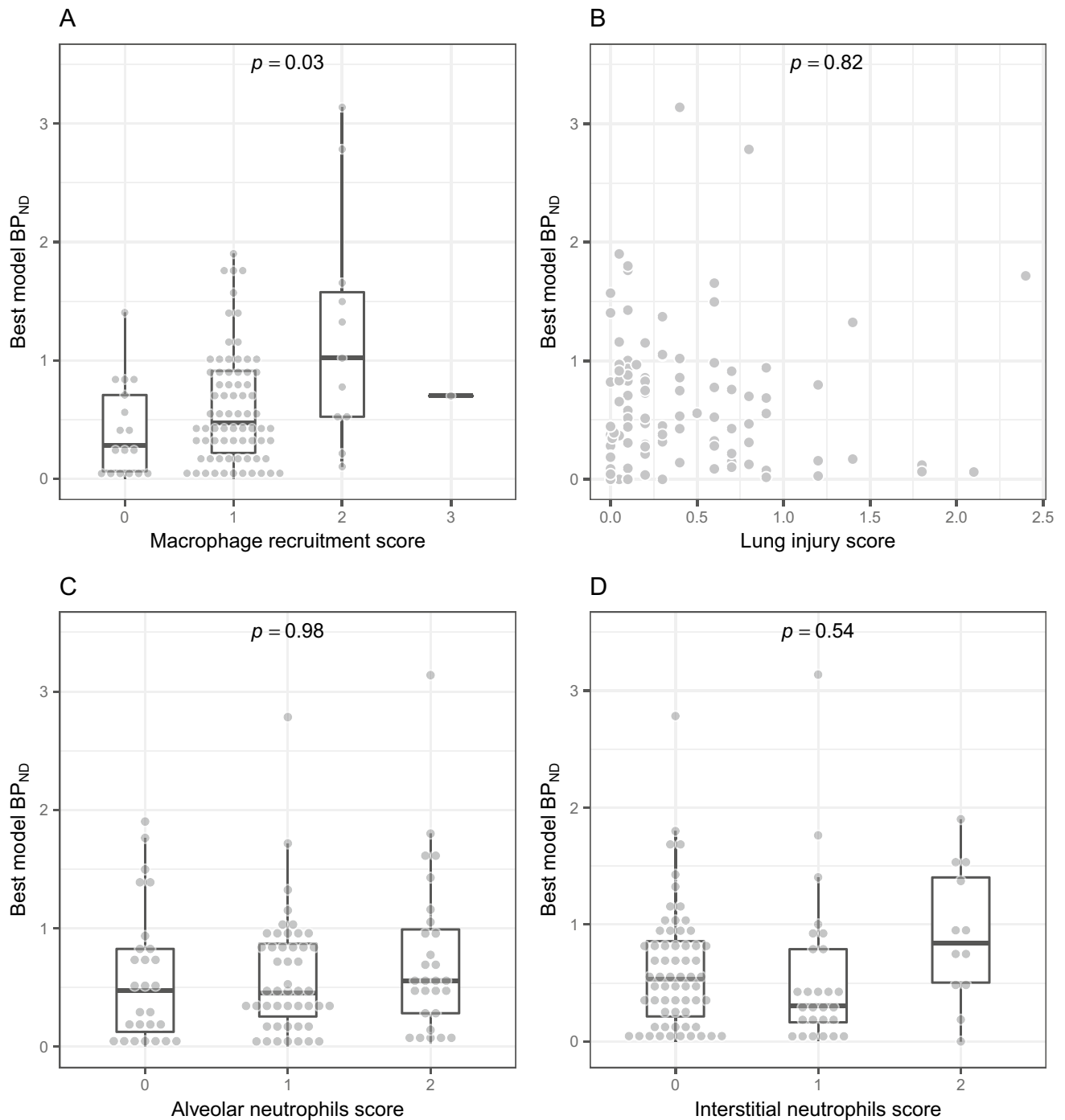


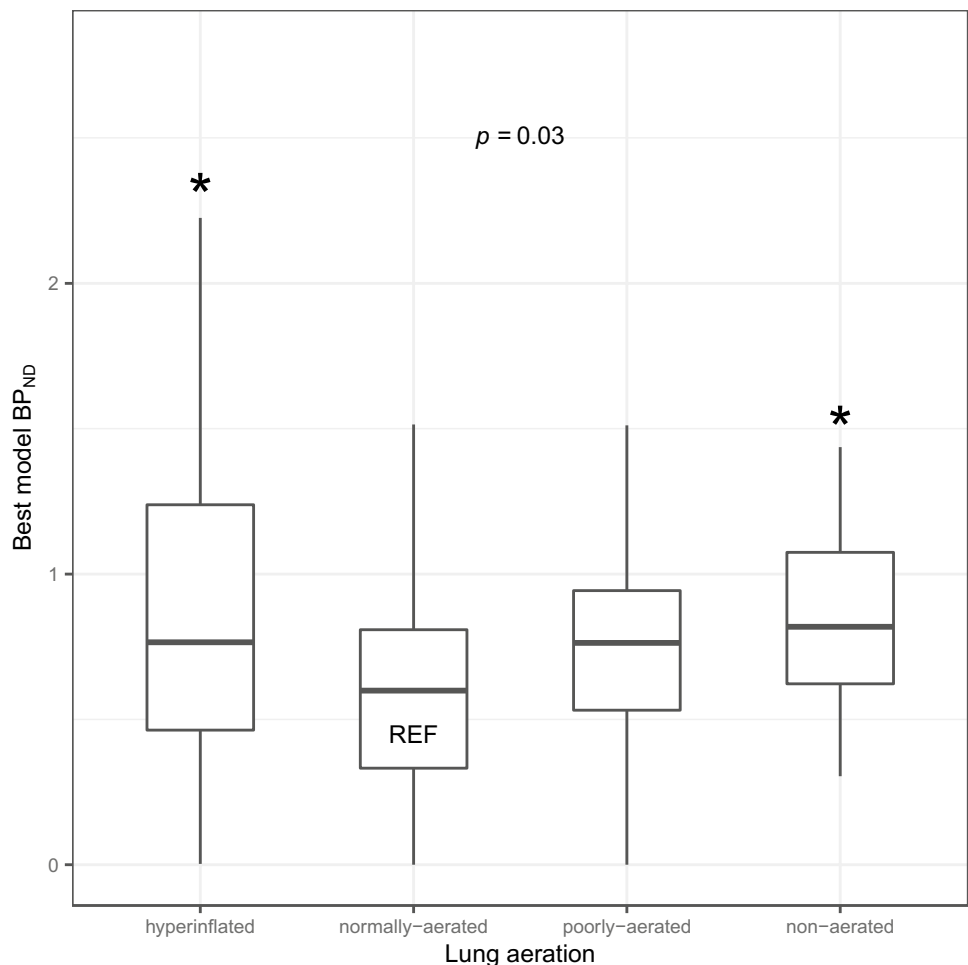
**Fig. 7** Association of [ $^{11}\text{C}$ ](R)-PK11195 binding potential with lung pathology scores. The figure shows regional best model  $BP_{ND}$  values (gray dots) quantified at T2 as a function of the macrophage recruitment score (panel **A**), of the lung injury score (panel **B**), and of the

alveolar and interstitial neutrophil counts (panels **C** and **D**). The  $p$  value examines the linear association of pathology scores with  $BP_{ND}$  regional values.  $BP_{ND}$ , binding potential

microparameter values determined by the 2TCM. Multiple factors may explain the benefits of adding a third, irreversible, and non-specific compartment to the kinetic model of [ $^{11}\text{C}$ ](R)-PK11195 lung uptake. First, [ $^{11}\text{C}$ ](R)-PK11195 is a highly lipophilic compound, thought to diffuse quickly in

tissues. Recent data suggests that the synthetic parent compound PK11195 may interact with planar lipid bilayer membranes and be trapped in between [9]. This would explain the non-specific uptake in tissues previously reported in studies that used the 2-tissue compartment reversible model to

**Fig. 8** Association of [ $^{11}\text{C}$ ] (R)-PK11195 binding potential with lung aeration. The figure shows boxplots of best model  $\text{BP}_{\text{ND}}$  as a function of 4 lung aeration levels: hyperinflated, normally, poorly, and non-aerated. The normally aerated compartment was defined as the reference compartment. The  $p$  value indicates the result of the overall association of aeration levels with best model  $\text{BP}_{\text{ND}}$  (\*:  $p < 0.05$  versus the reference level, Dunnett test).  $\text{BP}_{\text{ND}}$ , binding potential



describe [ $^{11}\text{C}$ ](R)-PK11195 kinetics in the brain or joints [3, 7]. This phenomenon had already been suspected by Kropf et al., who concluded that it would inevitably lead to the overestimation of  $\text{BP}_{\text{ND}}$  [7]; this we confirmed in our simulation study where we observed a mean  $\text{BP}_{\text{ND}}$  bias of 27% if the 2TCM was applied. Future research will need to confirm the existence of this compartment in histology.

Importance of the non-specific uptake of the tracer is confirmed by the association of  $\text{BP}_{\text{ND}}$  computed using the best model with the semi-quantitative score of macrophage presence in lung tissues, which was not the case when using exclusively the 2TCM to compute  $\text{BP}_{\text{ND}}$ . Also, model quality of fit was improved by the addition of  $k_5$  to the model, with a linear association between  $k_5$  and improved fit quality.

Model selection based on our algorithm led to the selection of the 3TCM in more than two-thirds of ROIs. In most cases, model selection was based on the lowest AICc value and not on the negligible 2TCM  $k_4$  value. Although infrequent, it is in our sense justified to select the 3TCM over the 2TCM, despite its higher AICc, when 2TCM  $k_4$  was so low that it should be assimilated to an irreversible uptake in the second compartment, probably due to image noise. Indeed,

we interpret the irreversible uptake that it implies as the consequence of an unaccounted-for extra compartment by the 2TCM in which the tracer is trapped irreversibly. Indeed, we observed  $k_5$  values significantly different from 0 in the subset of 3TCM-type ROIs classified using this criterion, supporting the relevance and impact of the third compartment on tracer quantification.

The best model  $\text{BP}_{\text{ND}}$  showed acceptable association with the macrophage pathology score, sufficient to help quantify non-invasively the course of macrophagic inflammation in this experimental setting. However, the model-determined parameters were not evaluated against direct quantification of the compound target, that is, the TSPO receptor (using ELISA for example). This also implies that we cannot assert without doubt that some of the uptake quantified by the  $\text{BP}_{\text{ND}}$  was not at least partly non-specific. Indeed, TSPO may be expressed by other cell lines (neutrophils, monocytes, type 2 alveolar cells) which play a key role in inflammatory states, which would have participated in non-specific uptake of the studied radioligand [23, 24]. However, we did not observe a significant association of model results with neutrophil infiltration of lung tissues. Some have also

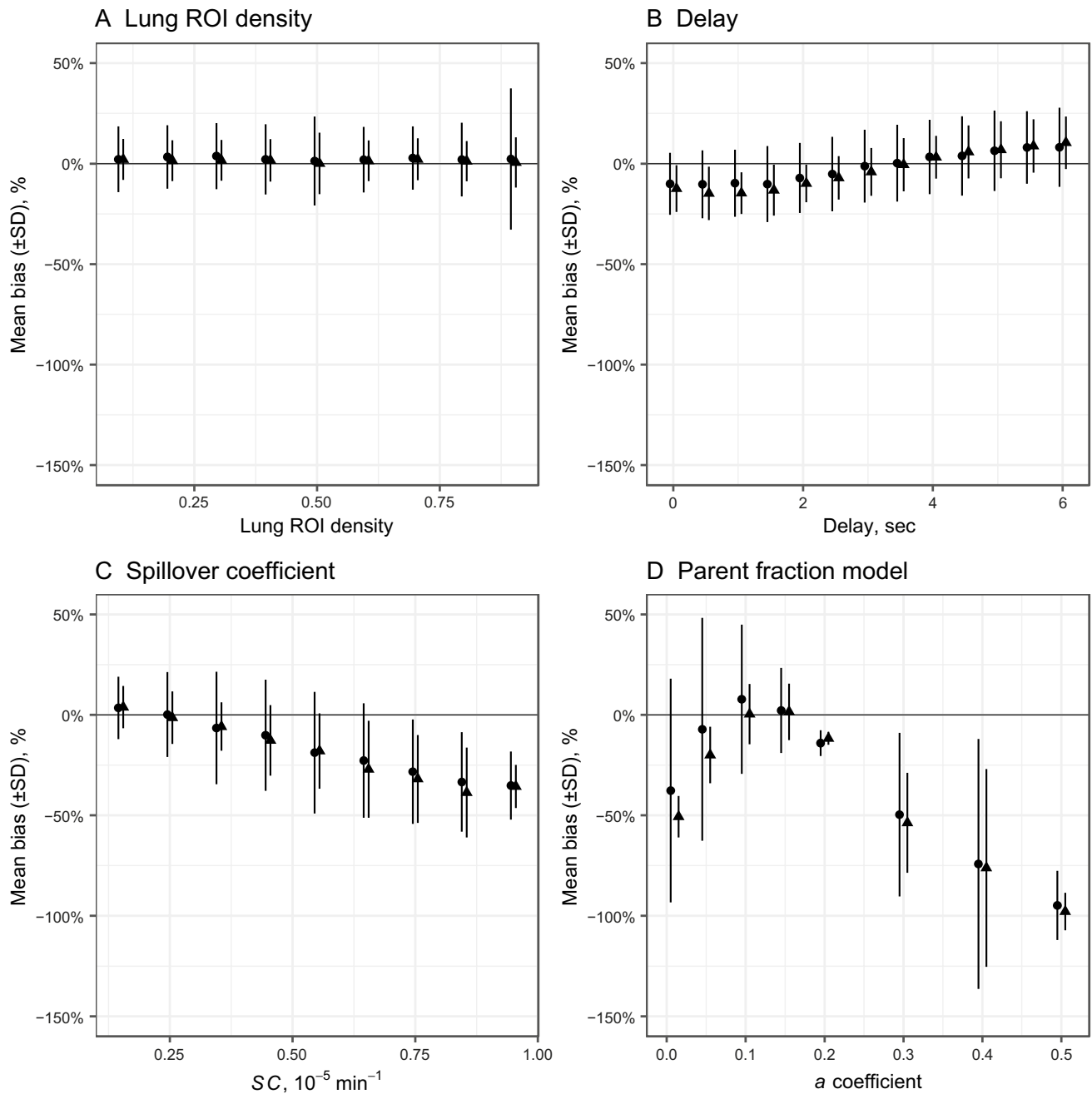


**Fig. 9** [ $^{11}\text{C}$ ](R)-PK11195 binding potential bias estimated with simulation studies. The figure shows the bias in simulated  $BP_{ND}$  across a realistic range of values of lung ROI density (**A**), regional arrival delay (**B**), spillover coefficient (**C**), and parent compound fraction (**D**), at 2 levels of Gaussian noise (5% represented by triangles, 10% with dots). The simulation was performed using thousands fit runs performed on an ideal tissue time-activity curve generated with the coefficients obtained using an ideal input function, to which a 5% or a 10% Gaussian noise was added. For each parameter of interest, we

varied the variable of interest over a given range: 0.1 to 0.9 fraction for lung ROI density, 0 to 6 s for regional arrival delay, 0th to 90th percentile value for SC, and 0.01 to 0.5 for the  $\alpha$  coefficient of the parent fraction fit. Bias was estimated as the difference between the simulated  $BP_{ND}$  and the ideal  $BP_{ND}$ , normalized to the ideal  $BP_{ND}$  value (relative bias). The figure shows the mean value of bias with its standard deviation for each value of the studied variable.  $BP_{ND}$ , binding potential;  $F_D$ , lung ROI density; SC, spillover coefficient; SD, standard deviation

demonstrated that the specificity of [ $^{11}\text{C}$ ](R)-PK11195 for TSPO and macrophages is high in the context of lung inflammation [24, 25]. As this may differ from the results of others,

we hypothesize that it may be the result of varying radioligand affinity for TSPO across species, or different affinity of TSPO radioligands ([ $^{11}\text{C}$ ](R)-PK11195, [ $^{11}\text{C}$ ]-PBR28, or

[ $^{18}\text{F}$ ]-FEDAC) for the TSPO protein [23, 24]. Also, TSPO expression and [ $^{11}\text{C}$ ](R)-PK11195 lung uptake in our experiments may have been increased not only due to inflammation triggered by our experimental settings, but also due to other stimuli such as renin-angiotensin system activation or adrenal upregulation [26]. However, this would only limitedly impact our results, as we mainly compared models applied to the same ROI.

Simulations showed that the best model  $\text{BP}_{\text{ND}}$  was only limitedly affected by noise, and not by errors in lung ROI density. The fact that ROI density did not generate a significant bias in  $\text{BP}_{\text{ND}}$  computation is of major importance, as it is pivotal issue in lung PET studies, with no uncontroversial method to adjust for its impact [18]. Furthermore, it provides a solution that is superior in robustness compared to the computation of regional SUV, even if the latter is corrected for regional lung densities. Also, our results show that  $F_{\text{D}}$ -corrected SUV cannot predict with sufficient quality the uptake of [ $^{11}\text{C}$ ](R)-PK11195. Indeed, regional SUV does not account for the quantity of blood present in the ROI, nor for the specific binding of the tracer to its receptor. Hence, our methodology offers the opportunity of quantifying tracer binding with relative independence from the presence of gas and blood in the studied ROI.

An unexpected finding of our work is the relatively high values of  $K_1$  computed with both models, compared to previously published work, more than 10 times higher than values previously reported in the brain [7]. First, this may be explained by the increase in tissue permeability and/or regional lung perfusion induced by acute inflammation in our model, as compared to chronic inflammatory states that are usually studied with [ $^{11}\text{C}$ ](R)-PK11195 PET [3–7]. Against this hypothesis is the fact that we observed significantly lower  $K_1$  values in animals with experimental ARDS compared to uninjured animals, although we cannot eliminate the potential impact on the pulmonary circulation of hypoxia or ventilatory parameters such as high PEEP. Second, high  $K_1$  values may be the consequence of the very large available surface of transfer between plasma and tissue in the lung, in direct relationship with the fact that it is the sole organ to receive 100% of blood flow. Third, it is possible that the computed  $K_1$  may have been affected and overestimated by the radiotracer's dispersion in the pulmonary vasculature [27], an error well-described in PET brain studies, although of lesser amplitude.

Despite our efforts to optimize initial guesses for model resolution, fit results produced very high values of  $k_3$  in a limited number of ROIs. Errors in microparameter determination are a well-known issue of PET modeling, especially present in brain [ $^{18}\text{F}$ ]-fluorodeoxyglucose studies, which does not usually impact the value of macroparameters such as  $\text{BP}_{\text{ND}}$  derived thereof [16]. Different methods exist to decrease the dispersion and variability of determined

microparameters, including optimization of initial guesses and adaptive weighed nonlinear resolution [16].

Quantification of [ $^{11}\text{C}$ ](R)-PK11195 metabolites required the use of a population-based fit, due to the logistic and technical difficulty to obtain individual curves at each PET acquisitions. Like in humans, we observed fast metabolization of [ $^{11}\text{C}$ ](R)-PK11195, with 15% of parent compound remaining at 60 min of PET study start [6]. Simulations showed that accounting for metabolization is of major importance, and that overestimation of the parent fraction would lead to substantial underestimation of  $\text{BP}_{\text{ND}}$ . Referencing  $\text{BP}_{\text{ND}}$  to the circulating plasma parent fraction would help decrease this error, similar to the computation of  $\text{BP}_{\text{F}}$ , i.e., the ratio of bound radioligand concentration to free ligand concentration in tissue, assuming that it is in equilibrium with plasma [10]. Finally, we hypothesize that the suspected error induced by increases in metabolization would only limitedly impact model results, as it would draw parent fraction towards lower values at equilibrium. This is in line with the conclusions of Lamare et al. and Kropholler et al. in humans [3, 6].

Several limitations must also be addressed. First, it must be notified that several factors may have impacted goodness-of-fit or model results, among which is the potential increase in TSPO expression over the course of PET acquisitions performed shortly after ARDS induction in protocol 2. However, because we compared the kinetic models in the same animal and ROIs, the bias would then have been identically applied to both models. Second, the specificity of [ $^{11}\text{C}$ ](R)-PK11195 binding to macrophage-bearing TSPO would have been further supported by microautoradiographic studies of lung macrophages in the presence of the radioligand. Third, we did not apply respiratory gating to PET acquisitions, which may have led extra-pulmonary TSPO-expressing tissues (such as cardiomyocytes) to enter the field of view. This would however have increased the duration of acquisitions, or, if it was kept constant, would have increased the image noise. Finally, [ $^{11}\text{C}$ ](R)-PK11195 is the first TSPO radioligand and is known for its low signal-to-noise ratio. However, this TSPO radioligand is most widely used, and other, although more recent, radioligands may lack specificity across species or in case of target protein polymorphism [28].

## Conclusions

To assess acute macrophagic lung inflammation in the context of experimental ARDS, PET quantification of [ $^{11}\text{C}$ ](R)-PK11195 lung uptake was significantly improved using a three-tissue compartment kinetic model, accounting for a non-specific and irreversible binding of the radiotracer in tissues. Combined with quantitative CT acquisitions, this



new methodology offers the opportunity to non-invasively explore mechanisms of ARDS and ventilator-induced lung injuries, and evaluate innovative strategies aiming to control acute lung inflammation.

**Supplementary Information** The online version contains supplementary material available at <https://doi.org/10.1007/s00259-022-05713-z>.

**Acknowledgements** The authors are grateful to Frederic Bonnefoi, Thibaut Jecker, Christian Tourvieuille, Franck Lavenne, Jérôme Redouté, and Jean-Baptiste Langlois, all at Centre d'Etude et de Recherche Multimodal et Pluridisciplinaire (CERMEP), for their help.

**Author contribution** LB designed the study; collected, analyzed, and interpreted the data; and drafted the manuscript. FD collected and analyzed the data. SL collected and analyzed the data and made substantial revisions to the manuscript for important intellectual content. DLB collected and analyzed the data and made substantial revisions to the manuscript for important intellectual content. NC interpreted the data and made substantial revisions to the manuscript for important intellectual content. NB analyzed and interpreted the data and made substantial revisions to the manuscript for important intellectual content. MO interpreted the data and made substantial revisions to the manuscript for important intellectual content. JCR designed the study; collected, analyzed, and interpreted the data; and made substantial revisions to the manuscript for important intellectual content. All authors approved the final version of the manuscript and agree to be accountable for all aspects of the work.

**Funding** The present work was funded by grants of the Société de Réanimation de Langue Française (Bourse de Recherche Expérimentale), and of the Hospices Civils de Lyon (Bourse Jeune Chercheur 2019).

**Data availability** Data will be made available upon reasonable request.

**Code availability** Code will be made available upon reasonable request.

## Declarations

**Ethics approval** The protocols were approved by an animal ethics committee (CELYNE, reference no. 2015041015179195 and 201907311141381).

**Consent to participate** Not applicable.

**Consent for publication** Not applicable.

**Conflict of interest** The authors declare no competing interests.

## References

- Jones HA, Valind SO, Clark IC, Bolden GE, Krausz T, Schofield JB, et al. Kinetics of lung macrophages monitored in vivo following particulate challenge in rabbits. *Toxicol Appl Pharmacol*. 2002;183:46–54.
- Pugliese F, Gaemperli O, Kinderlerer AR, Lamare F, Shalhoub J, Davies AH, et al. Imaging of vascular inflammation with [11C]-PK11195 and positron emission tomography/computed tomography angiography. *J Am Coll Cardiol*. 2010;56:653–61. <https://doi.org/10.1016/j.jacc.2010.02.063>.
- Kropholler MA, Boellaard R, Elzinga EH, van der Laken CJ, Maruyama K, Kloet RW, et al. Quantification of (R)-[11C]PK11195 binding in rheumatoid arthritis. *Eur J Nucl Med Mol Imaging*. 2009;36:624–31. <https://doi.org/10.1007/s00259-008-0987-7>.
- van der Laken CJ, Elzinga EH, Kropholler MA, Molthoff CF, van der Heijden JW, Maruyama K, et al. Noninvasive imaging of macrophages in rheumatoid synovitis using 11C-(R)-PK11195 and positron emission tomography. *Arthritis Rheum*. 2008;58:3350–5. <https://doi.org/10.1002/art.23955>.
- Jucaite A, Cselenyi Z, Arvidsson A, Ahlberg G, Julin P, Varnas K, et al. Kinetic analysis and test-retest variability of the radioligand [11C](R)-PK11195 binding to TSPO in the human brain - a PET study in control subjects. *EJNMMI Res*. 2012;2:15. <https://doi.org/10.1186/2191-219X-2-15>.
- Lamare F, Hinz R, Gaemperli O, Pugliese F, Mason JC, Spinks T, et al. Detection and quantification of large-vessel inflammation with 11C-(R)-PK11195 PET/CT. *J Nucl Med*. 2011;52:33–9. <https://doi.org/10.2967/jnumed.110.079038>.
- Kropholler MA, Boellaard R, Schuitemaker A, van Berckel BN, Luurtsema G, Windhorst AD, et al. Development of a tracer kinetic plasma input model for (R)-[11C]PK11195 brain studies. *J Cereb Blood Flow Metab*. 2005;25:842–51. <https://doi.org/10.1038/sj.jcbfm.9600092>.
- Bitker L, Costes N, Le Bars D, Lavenne F, Orkisz M, Hernandez Hoyos M, et al. Noninvasive quantification of macrophagic lung recruitment during experimental ventilation-induced lung injury. *J Appl Physiol*. 1985;2019(127):546–58. <https://doi.org/10.1152/jappphysiol.00825.2018>.
- Hatty CR, Le Brun AP, Lake V, Clifton LA, Liu GJ, James M, et al. Investigating the interactions of the 18kDa translocator protein and its ligand PK11195 in planar lipid bilayers. *Biochim Biophys Acta*. 2014;1838:1019–30. <https://doi.org/10.1016/j.bbame.2013.12.013>.
- Innis RB, Cunningham VJ, Delforge J, Fujita M, Gjedde A, Gunn RN, et al. Consensus nomenclature for in vivo imaging of reversibly binding radioligands. *J Cereb Blood Flow Metab*. 2007;27:1533–9. <https://doi.org/10.1038/sj.jcbfm.9600493>.
- Golla SSV, Adriaanse SM, Yaqub M, Windhorst AD, Lamertsmas AA, van Berckel BNM, et al. Model selection criteria for dynamic brain PET studies. *EJNMMI Phys*. 2017;4:30. <https://doi.org/10.1186/s40658-017-0197-0>.
- Matute-Bello G, Downey G, Moore BB, Goshong SD, Matthay MA, Slutsky AS, et al. An official American Thoracic Society workshop report: features and measurements of experimental acute lung injury in animals. *Am J Respir Cell Mol Biol*. 2011;44:725–38. <https://doi.org/10.1165/rcmb.2009-0210ST>.
- Hashimoto K, Inoue O, Suzuki K, Yamasaki T, Kojima M. Synthesis and evaluation of 11C-PK 11195 for in vivo study of peripheral-type benzodiazepine receptors using positron emission tomography. *Ann Nucl Med*. 1989;3:63–71.
- Gattinoni L, Caironi P, Cressoni M, Chiumello D, Ranieri VM, Quintel M, et al. Lung recruitment in patients with the acute respiratory distress syndrome. *N Engl J Med*. 2006;354:1775–86. <https://doi.org/10.1056/NEJMoa052052>.
- Gattinoni L, Pesenti A, Bombino M, Baglioni S, Rivolta M, Rossi F, et al. Relationships between lung computed tomographic density, gas exchange, and PEEP in acute respiratory failure. *Anesthesiology*. 1988;69:824–32.
- Huang S-C, Wu L-C, Lin W-C, Lin K-P, Liu R-S. Adaptive weighted nonlinear least squares method for fluorodeoxyglucose positron emission tomography quantification. *J med biol eng*. 2018;38:63–75. <https://doi.org/10.1007/s40846-017-0313-6>.

17. van den Hoff J, Oehme L, Schramm G, Maus J, Lougovski A, Petr J, et al. The PET-derived tumor-to-blood standard uptake ratio (SUR) is superior to tumor SUV as a surrogate parameter of the metabolic rate of FDG. *EJNMMI Res.* 2013;3:77. <https://doi.org/10.1186/2191-219x-3-77>.
18. Lambrou T, Groves AM, Erlandsson K, Screatton N, Endozo R, Win T, et al. The importance of correction for tissue fraction effects in lung PET: preliminary findings. *Eur J Nucl Med Mol Imaging.* 2011;38:2238–46. <https://doi.org/10.1007/s00259-011-1906-x>.
19. Schroeder T, Vidal Melo MF, Musch G, Harris RS, Venegas JG, Winkler T. Image-derived input function for assessment of 18F-FDG uptake by the inflamed lung. *J Nucl Med.* 2007;48:1889–96. <https://doi.org/10.2967/jnumed.107.041079>.
20. Broccard AF, Shapiro RS, Schmitz LL, Ravenscraft SA, Marini JJ. Influence of prone position on the extent and distribution of lung injury in a high tidal volume oleic acid model of acute respiratory distress syndrome. *Crit Care Med.* 1997;25:16–27.
21. R Development Core Team. R: a language and environment for statistical computing. Vienna, Austria: R Foundation for Statistical Computing; 2008.
22. Chen DL, Cheriyan J, Chilvers ER, Choudhury G, Coello C, Connell M, et al. Quantification of lung PET images: challenges and opportunities. *J Nucl Med.* 2017;58:201–7. <https://doi.org/10.2967/jnumed.116.184796>.
23. Hatori A, Yui J, Yamasaki T, Xie L, Kumata K, Fujinaga M, et al. PET imaging of lung inflammation with [18F]FEDAC, a radioligand for translocator protein (18 kDa). *PLoS ONE.* 2012;7:e45065. <https://doi.org/10.1371/journal.pone.0045065>.
24. Chen DL, Agapov E, Wu K, Engle JT, Solingapuram Sai KK, Arentson E, et al. Selective imaging of lung macrophages using [(11)C]PBR28-based positron emission tomography. *Mol Imaging Biol.* 2021. <https://doi.org/10.1007/s11307-021-01617-w>.
25. Jones H. Kinetics of lung macrophages monitored in vivo following particulate challenge in rabbits. *Toxicol Appl Pharmacol.* 2002;183:46–54. <https://doi.org/10.1006/taap.2002.9462>.
26. Batarseh A, Papadopoulos V. Regulation of translocator protein 18 kDa (TSPO) expression in health and disease states. *Mol Cell Endocrinol.* 2010;327:1–12. <https://doi.org/10.1016/j.mce.2010.06.013>.
27. Clough AV, Haworth ST, Hanger CC, Wang J, Roerig DL, Linehan JH, et al. Transit time dispersion in the pulmonary arterial tree. *J Appl Physiol.* 1985;1998(85):565–74. <https://doi.org/10.1152/jappl.1998.85.2.565>.
28. Chauveau F, Becker G, Boutin H. Have (R)-[(11)C]PK11195 challenges fulfilled the promise? A scoping review of clinical TSPO PET studies. *Eur J Nucl Med Mol Imaging.* 2021. <https://doi.org/10.1007/s00259-021-05425-w>.

**Publisher's note** Springer Nature remains neutral with regard to jurisdictional claims in published maps and institutional affiliations.